applied mechanics

MDPI

Article

Continuous Feed Grinding Milling Process of Soda-Lime Glass Using Smoothed-Particle Hydrodynamics

Joshua Alamo [1], Jameson Pitcheralle [1], Craig G. Merrett [1], Michael C. F. Bazzocchi [1,2,*] and Marcias Martinez [1]

[1] Department of Mechanical and Aerospace Engineering, Clarkson University, 8 Clarkson Ave., Potsdam, NY 13699, USA; alamoj@clarkson.edu (J.A.); pitchejr@clarkson.edu (J.P.); cmerrett@clarkson.edu (C.G.M.); mmartine@clarkson.edu (M.M.)

[2] Department of Earth and Space Science and Engineering, York University, 4700 Keele Street, Toronto, ON M3J 1P3, Canada

* Correspondence: mbazz@yorku.ca or mbazzocc@clarkson.edu

Abstract: A smoothed-particle hydrodynamics (SPH) modeling technique was applied in conjunction with the Johnson–Holmquist (JH-2) ceramic material constitutive model to replicate the fracture of soda-lime glass in a milling manufacturing process. Four-point bending tests were conducted to validate the soda-lime glass bulk material properties prior to its implementation in ABAQUS CAE™ Explicit (Version 2017). The JH-2 material constitutive model replicated the fracture load and time to fracture for the four-point bending load cases as per ASTM C158. This study showed how SPH in combination with a validated JH-2 material model in a milling process simulation was able to replicate the output size distribution at 5000 and 6500 revolutions per minute (RPM). For operations at 3000 RPM or lower, it was shown that it is necessary to include additional effects in the model, such as fluid–structure interactions, to improve the correlation with the experimental data. The SPH model was validated through an experimental campaign using high-speed cameras and a particle Camsizer. The experimental results clearly indicate a direct relation between the mill's RPM and the output particle size distribution.

Keywords: smoothed-particle hydrodynamics; fracture with multiple interactions; soda-lime glass; milling process; Johnson–Holmquist constitutive model

Citation: Alamo, J.; Pitcheralle, J.; Merrett, C.G.; Bazzocchi, M.C.F.; Martinez, M. Continuous Feed Grinding Milling Process of Soda-Lime Glass Using Smoothed-Particle Hydrodynamics. *Appl. Mech.* **2024**, *5*, 58–72. https://doi.org/10.3390/applmech5010004

Received: 23 December 2023
Revised: 17 January 2024
Accepted: 19 January 2024
Published: 23 January 2024

1. Introduction

Glass is an essential material in many modern applications ranging from infrastructure to consumer goods, leading to an increased need to predict glass fracture during manufacturing processes. Glass fracture has been studied for over 100 years [1]; however, there is a lack of computational modeling of glass fracture with multiple interactions in a manufacturing setting. Glass beads are commonly used in reflective paints [2,3] and surface treatment processes [4]. Previous studies used finite element analysis [5], smoothed particle hydrodynamics (SPH) [6], and other techniques, such as multi-scale approaches [7], to capture the fracture of brittle materials with varying success. The computational models used for capturing the fracture of glass are largely limited to a single interaction involving a single piece of glass. In comparison, ductile material models have been developed and have been shown to model complex manufacturing and failure processes [8–10]. This study expands the use of SPH to capture the fracture of glass in a continuous-feed grinding milling process to determine if a computational approach can produce a relation between milling revolutions per minute (RPM) and the output particle size distribution.

The finite element method (FEM) and SPH are the two most common computational models used by engineers to simulate glass fracture. A study conducted by Pelfrene et al. investigated different damage models for soda-lime glass using FEM [5]. Their study focused on three distinct techniques: the first was immediate element deletion, the second was application of the Hillerborg model that made use of a smeared crack technique, while

the third was a crack delay model. Their study analyzed each of these techniques by using a circular glass plate struck by an impactor and compared the fracture pattern to experimental results. The study's first conclusion was that traditional Lagrangian finite element methods were not able to account for crack directionality. The authors also concluded that the energy dissipated by damage exceeded the fracture energy of the material if the element size was above a critical length [5].

The use of SPH is particularly suited for modeling a cortical drilling process by capturing material fracture without relying on element deletion, thus ensuring conservation of mass. In recent years, SPH has become increasingly common when modeling brittle materials that range from cortical bone to ceramics. A study conducted by Tajdari et al. compared the capabilities of SPH to FEM for modeling both ductile and brittle materials [11]. The ductile material chosen for their study was aluminum 2024-T351 and the brittle material chosen was cortical bone. The study focused on drilling, cutting, and four-point bending scenarios to test the capabilities of each technique. The drilling model was of particular interest as it involved the interactions of test cases. The study investigated both standard twist drilling and Kirschner (K-wire) drilling to analyze the different physical behaviors of the two processes. The study concluded that SPH offered superior performance in comparison to the FEM technique because of the capabilities of the technique to retain fractured particles in the model, thus allowing for continuous interaction with the other particles and parts of the model. The study also concluded that the effectiveness of SPH was dependent on the number of free surfaces in the model as the truncated kernel function from free surfaces affected the stiffness of the material [11].

Another study conducted by Nordendale et al. investigated the use of SPH for simulating brittle armor under blast loading conditions [7]. The study focused on cementitious materials that are used for constructing barricades in wartime scenarios. The study made use of SPH because of its ability to track particles throughout the domain without incurring additional computational cost, which is a deficiency of coupled Eulerian–Lagrangian models. Additionally, SPH is not affected by severely distorted elements that affect the traditional Lagrangian technique. The study made use of an improved constitutive model based on the Johnson–Holmquist (JH-2), and Drucker–Prager models to represent ashcrete material. The study found that the SPH model showed the appropriate fragmentation and spall behavior of the material as the impact occurred. The study also found that FEM developed a larger plastic strain throughout because of the target elements surrounding the projectile. The authors of the study also observed how SPH became more prominent when applied to multiple stacked panels since the particles continued to interact in the model once the fracture occurred. The study showed an increase of 4.5 times in computational cost when using SPH compared to FEM, which was highlighted as a major drawback of the technique. The study concluded that SPH sufficiently predicted the exit velocity of the projectile, accurately simulating the fragmentation of the panel [7]. A study conducted by Gordon Johnson and Tim Holmquist in 1994 defined a second revision of their material constitutive model for ceramics under high-strain or strain-rate loading conditions [12]. The model referred to as the JH-2 model accounted for gradual increases in damage throughout a simulation, where the original JH-1 model only accounted for damage once an element was completely damaged. Damage was accounted for as the sum of the plastic strain across each integration cycle and divided by the plastic strain to failure of the material. Another advantage of the JH-2 model is that the pressure and strength variables are normalized with respect to the Hugoniot elastic limit (HEL) that allows for dimensionless constants. The dimensionless constants allow for materials to be compared to each other when there are insufficient experimental data.

A study conducted by Meyland et al. investigated the use of the JH-2 model in simulating the fracture of glass in high strain-rate scenarios [13]. The study looked at a ring-on-ring impact scenario following ASTM C1499 [14] to compare the fracture patterns between computational models and experimental results. The study found that with the use of tetrahedral elements, the JH-2 constitutive model overestimated the fracture strength

of the glass with higher piston velocities. The JH-2 model also captured both compression and tensile loading cases. The authors concluded that the model was capable of producing accurate fracture patterns [13]. Tan et al. updated the strain-rate-dependent parameters of the JH-2 model using split-Hopkinson testing techniques in contrast to the flyer plate experiments of the original study [15]. The study used a combined shear-compression loading technique of the split-Hopkinson bar for quasi-static testing. Testing took place at various angles and compression speeds to ensure that the material parameters were accurate for a wide range of scenarios. During dynamic testing the maximum strain rate achieved was 200 s^{-1} and showed that the fracture strength increased as the strain rate increased. The authors concluded that the original material properties proposed by Johnson and Holmquist overestimated the strength of the glass. The study also concluded that the new proposed material model represented the dynamic response and material characteristics of soda-lime glass [15].

The literature review and state of the art evaluation revealed a lack of computational models for brittle fracture with multiple interactions in manufacturing milling processes. As part of this study, an experimental and computational campaign demonstrated the use of SPH for the milling of soda-lime glass during a continuous-feed grinding manufacturing milling process. This process is convoluted in nature, with multiple interactions, complex fracture mechanics and is computationally intensive. The primary objectives of this study were: (i) to identify a relation between the grinding speed and the particle output particle size distribution; and (ii) to determine the ability of SPH to replicate the complex behavior of a manufacturing grinding milling process for soda-lime glass. An experimental campaign validated the SPH model through the use of high-speed cameras to investigate the fracture dynamics of soda-lime glass and use of a Camsizer to evaluate the particle size distribution of the experimental results with respect to those obtained from the SPH model. Finally, this study showcased the use of novel post-processing techniques to compare the output of the SPH model and the experimental results.

2. Methodology

This study used a continuous-feed grinding drive with an impact grinding head IKA Model 2836001 from Cole-Parmer (Vernon Hills, IL, USA), as shown in Figure 1a [16]. A simplified SolidWorks™ 2023 CAD model of the laboratory mill was created, as shown in Figure 1b. A new cover was manufactured from stainless-steel 304 with soda-lime glass inserts to cover the windows where the cameras were located to visualize the fracture process inside the mill, as shown in Figure 1a. A new continuous-feed mechanism was 3D-printed and adapted to the cover. LED lights were attached directly to the inside of the front cover to ensure proper lighting during recording, while avoiding reflections from the glass windows.

All computational models were developed in ABAQUS CAE™ Explicit (Version 2022) [17]. All simulations were performed on two high-end computing systems. The first system was equipped with two Intel (Santa Clara, CA, USA) Xeon® Silver 4210R CPUs, while the second system was equipped with two Intel Xeon® E5-2650 v3 CPUs; both systems were equipped with 20 physical cores and 40 logical processors. In addition, the systems included an NVIDIA (Santa Clara, CA, USA) Quadro RTX 4000 GPU and an AMD FirePro 5100 GPU, respectively. Finally, both computing systems were equipped with 128 GB of RAM and over 10 TB of hard drive storage space.

This study focused on the implementation of an SPH computational model and used experimental results as validation for the computational results. To validate the SPH model, the study developed a computational campaign that ran in parallel to the experimental campaign. The following subsections aim to describe in detail the different aspects of the computational and experimental methods to determine the efficacy of the SPH method to simulate a glass fracture in a grinding milling process.

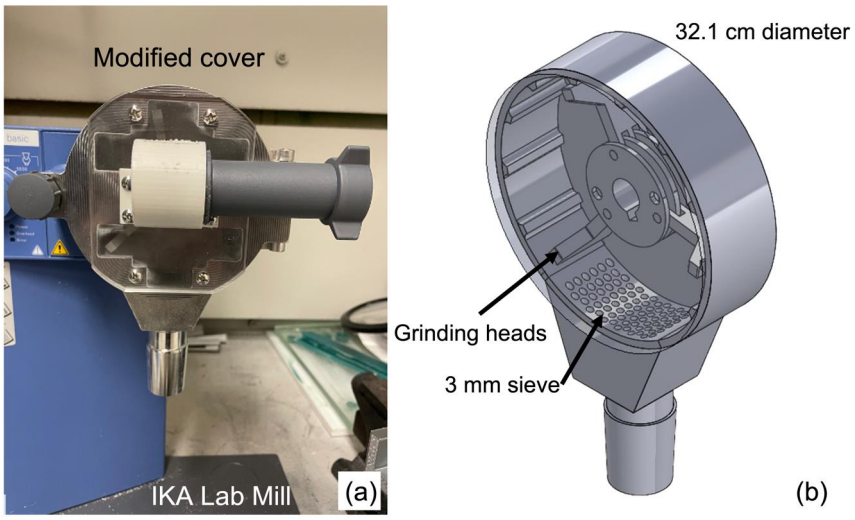

Figure 1. (**a**) IKA lab mill. (**b**) Simplified lab mill geometry in SolidWorks™.

2.1. Material Constitutive Model of Soda-Lime Glass

The material constitutive model chosen for the soda-lime glass was the Johnson–Holmquist (JH-2) material model that was specifically designed for ceramic fracture under high strain loading [4]. The material and modeling parameters for soda-lime glass used in this study are shown in Table 1 and were taken from experimental tests conducted by Tan et al. [15]. The material results outlined in Table 1 were implemented in every computational model conducted in this study. The material parameters outlined in Table 1 could not be independently verified by the authors, as the laboratory is not equipped with a split-Hopkinson test fixture.

Table 1. Soda-lime glass material and modeling parameters [15].

Property	Value	Property	Value
Density (kg/mm^3)	2.53×10^{-6}	HEL (MPa)	5950
Shear Modulus (MPa)	26,900	P_HEL (MPa)	2920
A	0.71	β	1.0
N	0.61	D_1	0.043
B	0.178	D_2	0.85
M	1.0	Initial Damage	0
C	0.00843/0.39165	K_1 (MPa)	43,200
$\dot{\epsilon}$	0.001/100	K_2 (MPa)	−67,200
T (MPa)	27.8	K_3 (MPa)	153,200

As such, the authors of this study implemented quasi-static four-point bending and tensile test models to compare the computational results (using Table 1 material data) with those obtained experimentally. Soda-lime glass to perform the experimental campaign was acquired from [18]. The manufacturer provided the mechanical and chemical properties of the glass for comparison. The chemical analysis of this soda-lime silica float glass provided by the manufacturer indicated an approximate chemical composition of: 72.6% SiO_2–silica, 13.9% Na_2O–soda, 8.4% CaO–calcium oxide, 3.9% MgO–magnesium oxide, 1.1% Al_2O_3–alumina, 0.6% K_2O–potassium oxide, 0.2% SO_3–sulfur trioxide, and 0.1% Fe_2O_3–iron oxide. The results of these tests served to build confidence in the implementation of the SPH/JH-2 lab mill computational model and experimental tests of the IKA Model 2836001 continuous-feed grinding drive with an impact grinding head, as shown in Figure 1b. All the experimental and computational tests were conducted at the Holistic Structural Integrity Process (HolSIP) laboratory at Clarkson University.

2.2. Four-Point Bending Computational Model and Experimental Tests

Computational models and experimental tests were developed and conducted as per ASTM C158 to validate the bulk bending behavior of soda-lime glass. A total of 30 specimens were tested from four different batches to allow for consideration of the quality of specimens between each batch. The geometry of the specimen is outlined in Figure 2a as per ASTM C158.

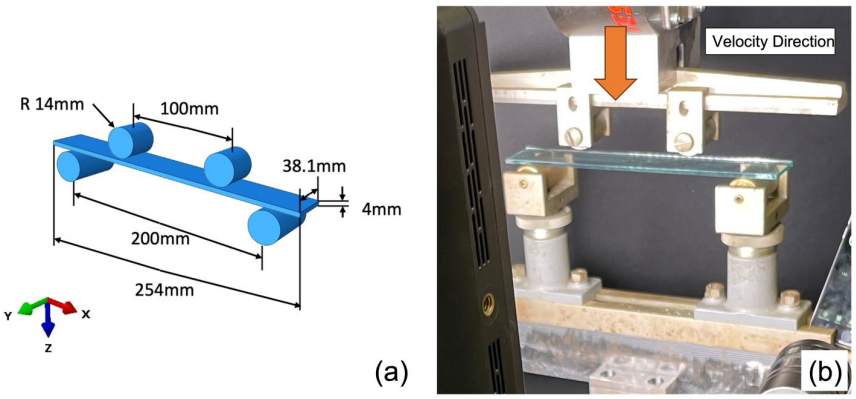

Figure 2. (**a**) Four-point bending computational assembly. (**b**) Experimental setup for four-point bending. All units in mm.

The rollers were modeled as discrete rigid parts as they do not deform during the testing. The test specimen was modeled as a deformable part with the soda-lime glass JH-2 material constitutive model. The JH-2 material model was implemented using the built-in user-defined material model by using "ABQ_JH2" in ABAQUS CAE™ [19]. The glass test specimen was meshed using tetrahedral elements with element deletion turned on to model the fracture. The lower rollers supporting the specimen were assigned encastre boundary conditions that prevented linear and rotational motion. The upper rollers used to apply the load were assigned boundary conditions to restrict rotational movement. A velocity boundary condition was applied to the upper rollers to replicate the loading direction of the experimental setup shown in Figure 2b.

The experiments were conducted on a 50 kN TestResources load frame connected to a Newton controller [20]. All data were recorded at a data acquisition rate of 100 Hz. High-speed cameras were positioned to capture the moment of failure of the specimen. A displacement rate of 2.5 mm/min was assigned to the Newton controller. A MATLAB® R2022a script was written to extract the data from the .csv files obtained during testing and to calculate the parameters set out by ASTM C158.

A statistical analysis was performed on the experimental data. The analysis focused on the maximum load [N], time [sec], rate of increase of maximum stress [MPa/sec], and the modulus of rupture [MPa]. The results were analyzed through boxplots in R-studio [21]. The boxplot calculations of the median, 1st quartile, 3rd quartile, and outliers were determined using Tukey's method [22]. Tukey's method of outlier detection defines an outlier as a data point that is outside of ±150% of the interquartile range.

2.3. Continuous-Feed Grinding Experimental and Computational Setup

The experimental setup used to evaluate the performance of SPH for modeling the complex phenomenon of a grinding milling process was performed on an IKA Model 2836001 continuous-feed grinding drive with an impact grinding head from Cole-Parmer [16], as shown in Figure 3a. In addition, the visualization of the fracture dynamics used two Chronos 2.1-HD high-speed cameras from Kron Technologies (Burnaby, BC, Canada) [23], also shown in Figure 3a. These two cameras were connected and synchronized to compare image frames (top and bottom windows in the mill). The experimental particle size distribution was determined using a Camsizer P4 from Microtrac MRB (York, PA, United States) [24].

The IKA Model 2836001 was designed to operate between 3000 RPM and 6500 RPM with the optimal range for impact grinding being 5000 to 6500 RPM. The grinding mill's operating speed was controlled to produce particles of different sizes as output; however, a 3 mm sieve mesh prevented particles 3 mm or larger from exiting the grinding mill. The glass fragments were collected as they exited the mill and post-processed using the Camsizer. The Camsizer reported the size of the glass particles that were used in the statistical analysis. In addition to the output particle size comparison, a direct visual comparison between the lab mill and computational model was performed using high-speed cameras and the ABAQUS CAE™ SPH results. The preliminary results showed insufficient lighting from the LED lights embedded in the cover. As such, to ensure proper contrast between the casing and the glass particles moving inside the mill, an additional external LED light was placed in front of the lid to increase the visibility inside the casing, as shown in Figure 3a.

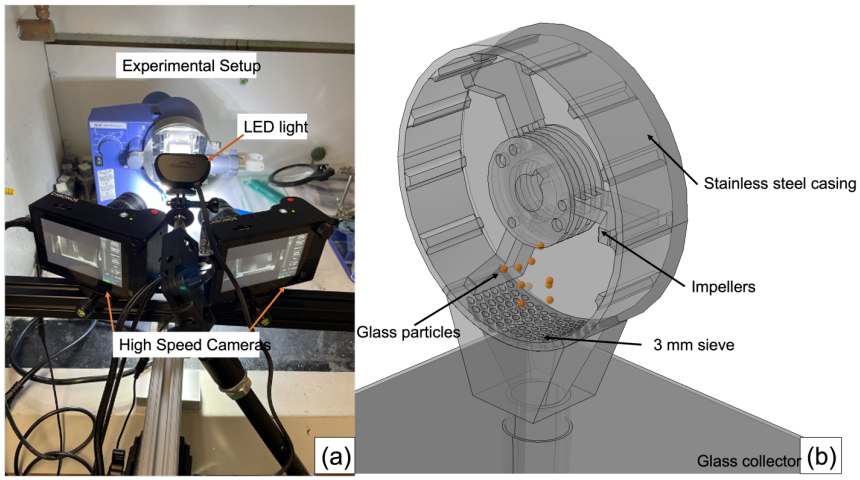

Figure 3. (**a**) Lab mill experimental setup. (**b**) ABAQUS CAE™ SPH computational model.

The computational model of the mill was developed in ABAQUS CAE™ Explicit, as shown in Figure 3b. The physical simulated time of the milling process varied between 0.05 and 0.25 s, which translated to over 600 h of computational time per simulation. The lab mill was modeled as rigid parts and was meshed using discrete rigid triangular elements to allow for the most uniform mesh across the complex geometries of the mill. The glass particles were meshed with C3D4 linear tetrahedral elements to allow for the SPH technique to be applied to the glass particles. The original particle size was set to 3 mm to mimic the approximate size of those used during the experimental campaign. This element type was chosen because of its stiff nature in comparison to hexahedral element types. The SPH particle size was set to 150 µm as anything smaller would translate to large computational simulation runs. The material constitutive model was applied to the glass in the same manner as that of the four-point bending and tensile test computational models (Table 1). All parts of the mill, except for the impeller were assigned rigid body constraints as boundary conditions to restrict their movement. To properly model the moment of inertia of the impeller, a preliminary model of a 304 stainless steel impeller was modeled in ABAQUS CAE™ Explicit. The moment of inertia tensor was computed from the model and assigned to the rigid impeller model. A rotational velocity boundary condition was applied to the impeller allowing the velocity to be matched to the experimental setup. Interaction properties for both the tangential and normal directions were applied to the model with "hard" contact in the normal direction and a coefficient of friction of 0.6 in the tangential direction [25]. Acceleration due to gravity was also applied to the entire model to ensure movement of the glass particles and fragmentation.

This study focused on comparing the mill operation at impeller speeds of 3000, 5000, and 6500 RPM, which meant the camera was set to record at 3000 frames per second (FPS)

with 1930 × 360 resolution and 5000 FPS with 1440 × 240 resolution. The recordings were saved at 1 FPS or as individual .TIFF images for playback and were analyzed to ensure that the entire impact sequence and milling process were captured. Still images from the high-speed camera were then compared to an approximate equivalent frame in the ABAQUS CAE™ Explicit model to examine the behavior of the computational model with respect to the experimental process.

2.4. Post-Processing Methodology of Computational Results

A statistical analysis of the size distribution from the lab mill was performed to validate the results of the computational model. A MATLAB® script was developed to analyze the ABAQUS odbReport for each computational simulation run at the different RPMs. Since all the particles in the SPH simulation have the same size, it was possible to estimate the size of each fragment by counting the number of particles that composed the fragment. The coordinates of each SPH particle were recorded in the odbReport and the distance between any two SPH particles was calculated. If the distance between SPH particles was less than the kernel domain size, then SPH particles were part of the same fragment. The script looped through each of the connected nodes to determine which other nodes made up the entire fragment. The distance between each node in the individual fragments was calculated, and the largest nodal distance within a fragment was recorded as the diameter of the fragment. The fragments were sorted into the respective bin based on the diameter to form the output size distribution. Bar plots were created for both the computational and experimental outputs and overlaid on a single figure for each respective speed. Cullen and Frey plots were created for both computational and experimental distributions for each speed to determine the shape, skewness, and kurtosis of the individual distributions. A Kolmogorov–Smirnov test was conducted to determine if the data formed part of the same distribution type [26].

3. Results and Discussion

The results of the study are divided into four subsections. The first two subsections are the results and discussion of the four-point bending and tensile tests, respectively. The third subsection is a visual comparison between the experimental lab mill and the computational model. The final subsection contains a statistical analysis of the size distribution of the output of the lab mill, focusing primarily on output particle sizes less than 149 microns that are considered waste product in this study.

3.1. ASTM C158 Four-Point Bending Results and Discussion

A total of 30 samples of soda-lime glass were tested in the four-point bending fixture. Figure 4 highlights the force versus time curve for some of the coupons tested. Not all the results were plotted to avoid clutter of the graph. As seen in this figure, there was a large scatter in the time to failure of the glass specimen. This scatter is not unusual, as it is well known that small imperfections on the edges of the glass coupons can lead to premature failure and, thus, a large scatter in the ultimate load and time to fracture. In addition, the results of the four-point bending experiments are summarized in boxplots that were created for the time, maximum load, modulus of rupture, and rate of increase of maximum stress shown in Figure 5. The boxplots show that there were two true outliers in the data that needed to be removed from the analysis. The outliers are depicted in the boxplots using the "o" symbol. The outliers were assumed to occur because surface defects in the specimen directly impacted the strength of the glass. After 30 tested samples, the mean modulus of rupture was determined to be 79.51 MPa, which was within 5% difference of the listed mean modulus of rupture of 83 MPa for heat-strengthened soda-lime glass [18]. From both the statistical and visual analysis, the time to failure, and the failure behavior of the computational model and experimental testing were compared. The mean time to failure for the experimental testing was found to be 70.3 s, with the time to failure in the

computational model being 66 s, i.e., a 5.7% difference. These variations in the results can be attributed to small changes in the chemical composition of the soda-lime glass.

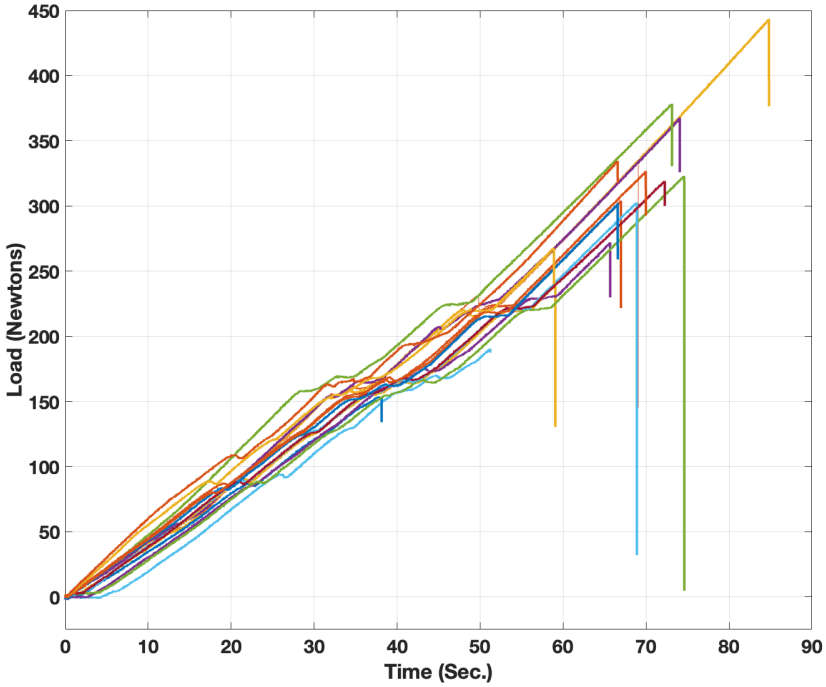

Figure 4. Typical experimental results load versus time. The colors are indicative of load versus time curves for different test coupons.

The computational model captured the fracture under each of the loading rollers but was incapable of capturing the sudden "explosion" of the glass fragments. The authors of this study also investigated the reaction force exerted on the loading roller to the maximum load exerted during the experimental tests. The computational model was expected to have a higher force than the experimental testing because the model does not account for the surface defects in the physical specimen. The maximum experimental force recorded was 580 N, while the computational model produced a maximum reaction force of 605 N, thus, a 6% difference between the computational and experimental results. The results of the four-point bending tests showed that the JH-2 constitutive model simulates the behavior of soda-lime glass accurately.

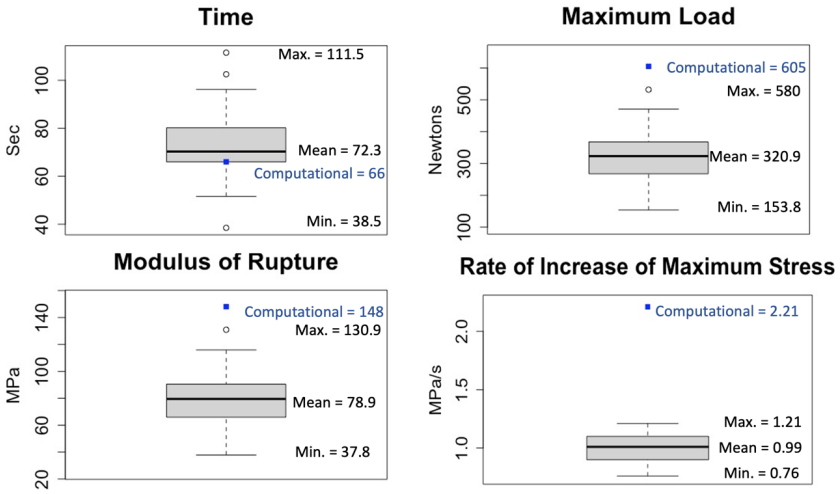

Figure 5. Boxplots for ASTM C158 experimental results.

3.2. Lab Mill Visual Comparison

The high-speed footage of the lab mill experimental operation was compared to the visual behavior of the computational model to provide a means of validating the SPH model. The experimental operation of the mill revealed that the glass particles initially bounce off the impeller and into the side of the lab mill where the fracture event occurred. This behavior was captured for 3000, 5000, and 6500 RPM experimental operations, as shown in Figure 6. Before obtaining this finding, it was hypothesized that the fracture occurred when the impeller interacted with the glass particles. As seen in Figure 6 (time 0.0 s), the glass particles fall from the feeder into the path of the incoming impeller, while at time 0.0052 s the impeller brushes past some of the particles. At time 0.0696 s, the passing impeller impacts the glass particles into the side wall casing where the fracture occurs. Fragments of smaller glass particles are clearly seen at 0.1388 and 0.23 s. As such, it was determined that the function of the impeller is to transfer the rotational energy to the glass particle causing this particle to strike the side walls of the mill at a higher impact velocity, thus creating fragmentation of the glass particles.

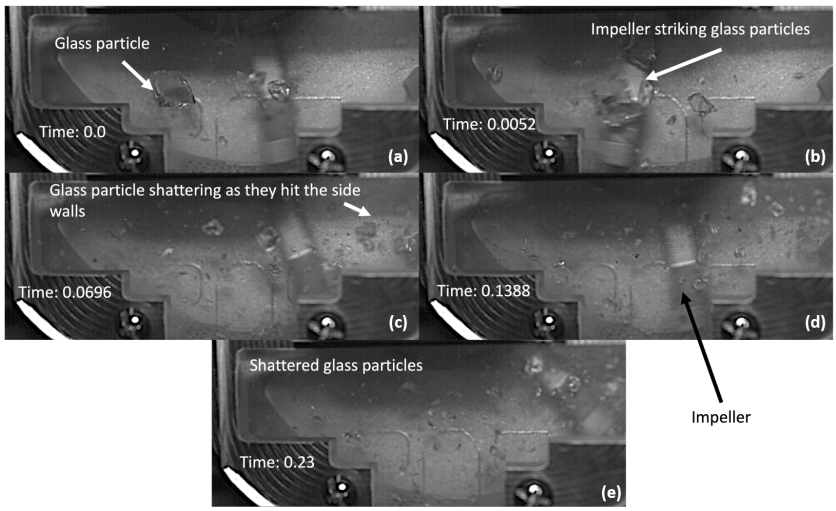

Figure 6. Lab mill experimental glass behavior at 5000 RPM. (**a**) Coarse glass particles enter the mill; (**b**) the impeller strikes the large coarse particles, causing the particles to swirl while other smaller particles are impacted and pushed to the side wall baffles; (**c**) the particles hitting the side walls are shattered causing smaller fragmentation of the glass particles; (**d**) subsequent impeller interactions continue to break the glass into smaller sizes; (**e**) the smaller fragments fall to the base of the mill and if sufficiently small (less than 3 mm in diameter) flow through the sieve into a collection box. All units of time are in seconds.

A similar set of results was visualized through the SPH computational model, as shown in Figure 7. At time zero, the particle fragments fall due to gravity into the incoming impeller. At 0.00125 s, some of the particles contact the impeller, but little fracture occurs. The impeller carries the particles and transfers the rotational energy to the particles. At time 0.00625 s, some of the particles hit the side walls causing the first indication of glass fracture. At time 0.02875 s, the incoming impellers hit the larger glass fragments and cause the fragments to hit the side walls multiple times. As the particles rotate around the casing, many of these fall to the bottom of the sieve and pass through the 3 mm diameter holes, thus dropping into the glass collection box.

It is important to state that for the 3000 RPM simulation results, many of the particles impacted by the impeller strike the side walls and partially break in a similar manner, as seen in the 5000 and 6500 RPM. As the glass particles rotate around the casing, they accumulate at the bottom of the sieve. These fragments are not allowed to pass the sieve because of their size. In contrast to the experimental results, in the computational model, the passing of the impellers does not cause any movement of the collected glass fragments

on the sieve. Thus, fragments sit undisturbed by the passing of the impeller. This effect at 3000 RPM was not experimentally seen through the high-speed cameras. In the high-speed camera footage, it was clearly shown how particles 3 mm in size or bigger are unable to pass through the sieve. However, these particles are moved by the airflow and, thus, continue to bounce and fracture around the casing.

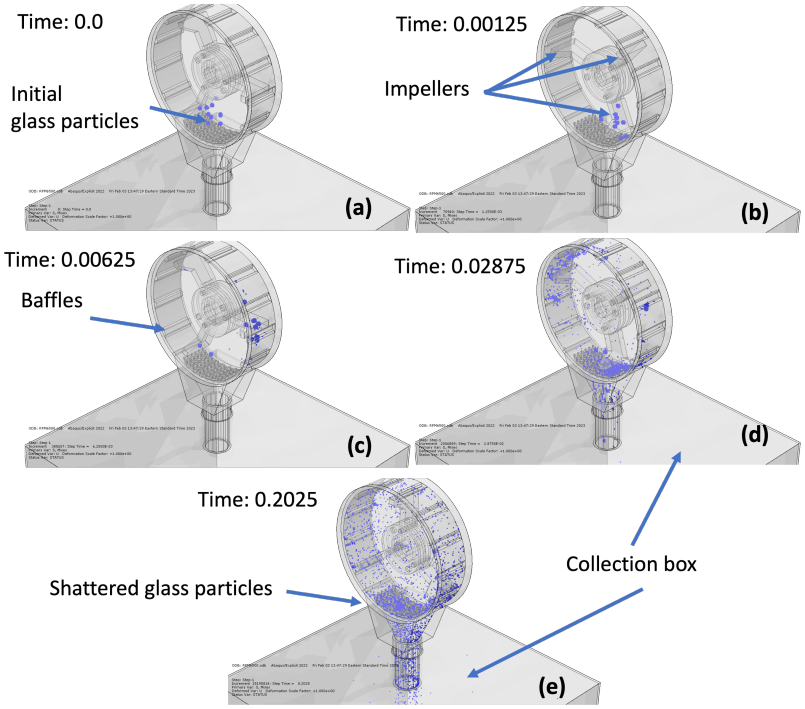

Figure 7. Lab mill computational model glass behavior at 5000 RPM. (**a**) Eight coarse glass particles (approximately 3 mm in size) modeled entering the mill; (**b**) impeller strikes the large coarse particles, causing the particles to impact the side wall baffles; (**c**) the particles hitting the side walls shatter causing smaller fragmentation of the glass particles, while others are pushed by the impeller to other sections of the mill; (**d**) subsequent impeller interactions continue to break the glass into smaller sizes; (**e**) the smaller fragments fall to the base of the mill and, if sufficiently small (less than 3 mm in diameter), flow through the sieve into a collection box. All units of time are in seconds.

The visualization of the fracture mechanisms clearly demonstrates how the fracture occurs inside the lab mill. As previously stated, the primary objective of this study was to determine a relation between the RPM and the glass particle size output distribution. In addition, the authors wanted to understand the formation of waste product, glass fragments that are smaller than 149 microns, thus considered as dust. These dust particles are too small for utilization in a production environment.

3.3. Glass Particle Output Size Distribution Results and Discussion

The statistical analysis of the glass particle output size distribution began with the creation of bar plots of the experimental and computational data. The size distribution comparison for the 3000 RPM operation is shown in Figure 8. The excess proportion of fragments in Bin #10 for the 3000 RPM operation is caused by a lack of fracture in the glass particles. Bin #1, for particles greater than 840 microns, forms 19% of the particles retained. Particles less than 149 microns constitute only 14% of the experimental results (waste). As seen in Figure 8, the computational model was unable to capture the experimental output distribution at 3000 RPM.

The output size distribution at the 5000 RPM operation of the lab mill is shown in Figure 9. The computational model was able to capture the size distribution and a shift in the mean that is evident in the experimental results from 3000 RPM to 5000 RPM. This shift

shows a large percentage of particles accumulated in Bin #10 from an experimental and computational perspective, indicating that a lower RPM may reduce waste production.

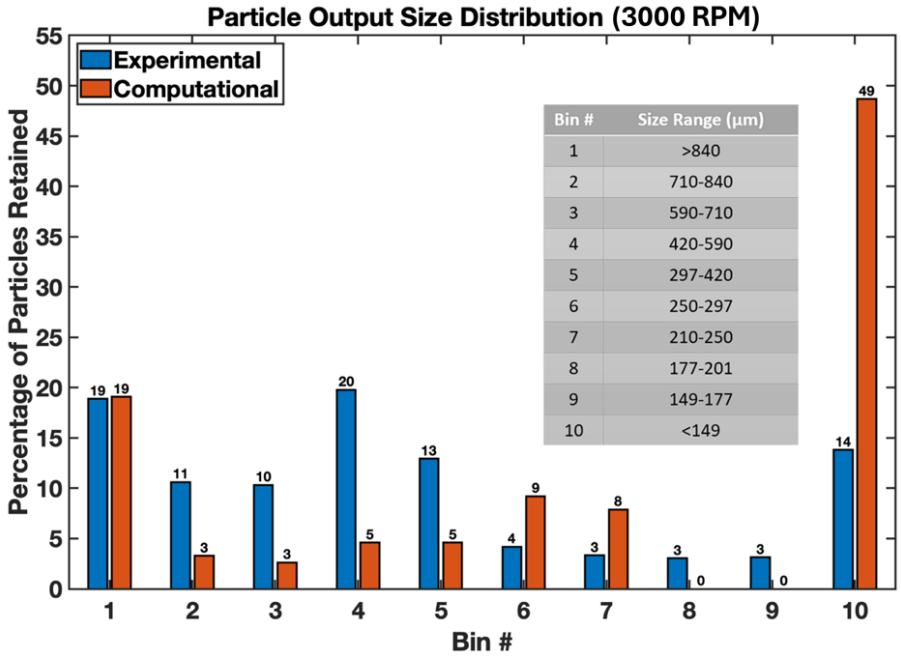

Figure 8. Lab mill output size distribution comparison for 3000 RPM.

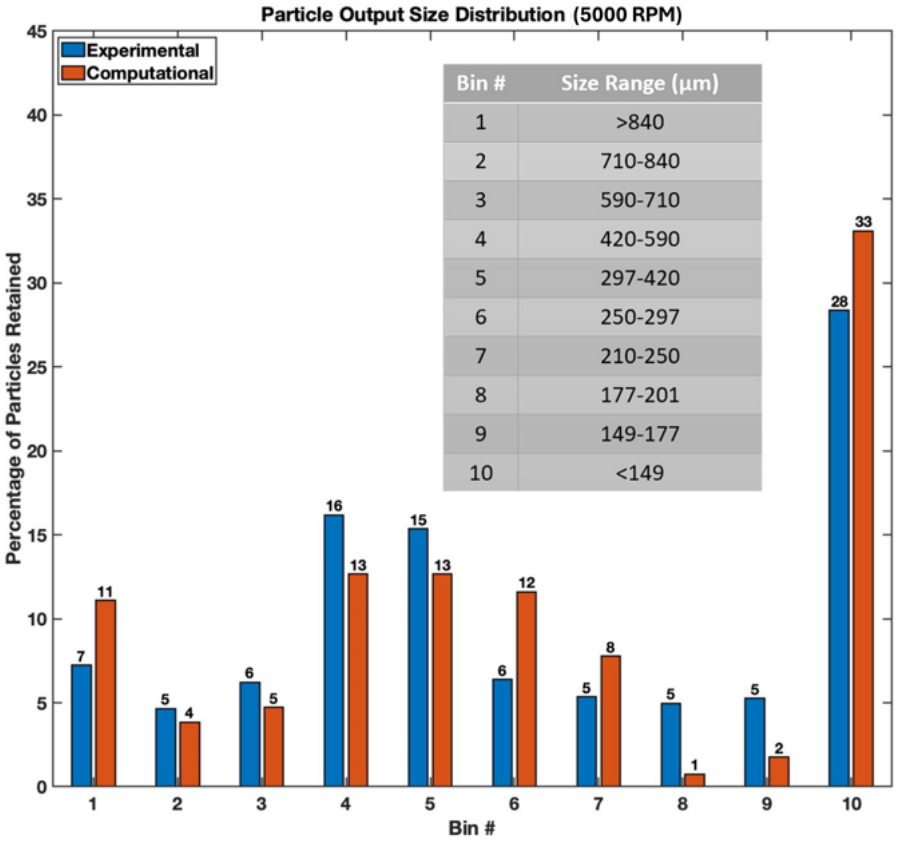

Figure 9. Lab mill output size distribution comparison for 5000 RPM.

The authors of this study hypothesize that, throughout a milling process, there is a transition point where aerodynamic effects no longer play a critical role in the behavior of the system. This transition point is dependent on the amount of energy the impeller

transfers to the glass fragments. For the lab mill, the transition point fell between 3000 and 5000 RPM, and was observed in the computational model. The transition could not be observed experimentally as there was no feasible way to place the lab mill in a vacuum.

The output size distribution for the 6500 RPM operation of the lab mill is shown in Figure 10. The size distribution produced by the lab mill trended towards a Weibull distribution with increasing skewness and kurtosis. The increasing skewness was caused by the increasing waste product (particles < 149 microns) in Bin #10 and the increasing kurtosis indicates the distribution becomes more focused about a single bin rather than multiple bins. Again, a faster RPM of the impeller seems to generate a greater percentage of dust particles (waste). It should be noted that, when comparing the computational and experimental distributions at all three operating speeds, the *p*-values were all above 0.05. This indicates that the datasets belong to the same distributions, and, consequently, the computational models provide an accurate representation of the milling process.

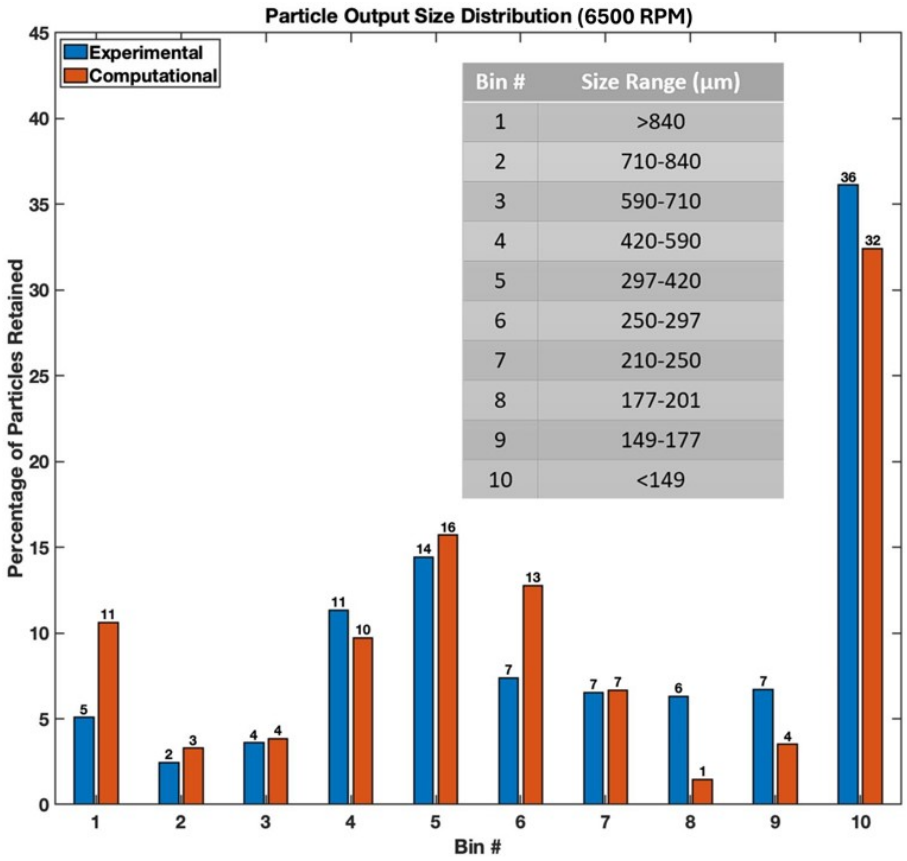

Bin #	Size Range (µm)
1	>840
2	710-840
3	590-710
4	420-590
5	297-420
6	250-297
7	210-250
8	177-201
9	149-177
10	<149

Figure 10. Lab mill output size distribution comparison for 6500 RPM.

Unfortunately, throughout the computational modeling portion of the study, it was observed that at slower speeds the momentum of the impeller was not enough to ensure the movement of the particles around the mill. To recreate the particle motion at the slower speeds, the authors hypothesize that fluid–structure interaction would be required (aerodynamic effects). Accounting for the aerodynamic effects is outside the scope of the current study but would be necessary for increasing the accuracy of the models at lower RPM.

Additionally, the mass of waste product in Bin #10 was compared at each of the operating speeds. It was hypothesized that the waste product made up a large percentage of the particles by number but accounted for a very small percentage of the mass in the system. The percentage of mass in Bin #10 for each scenario is shown in Figure 11. These results also demonstrate that the shape of the distribution shifts towards a Weibull distribution as the speed of the impeller increases. The skewness of the distribution also

increases as more fine material is produced. The kurtosis of the distribution increases as the peak becomes more focused around a single size bin.

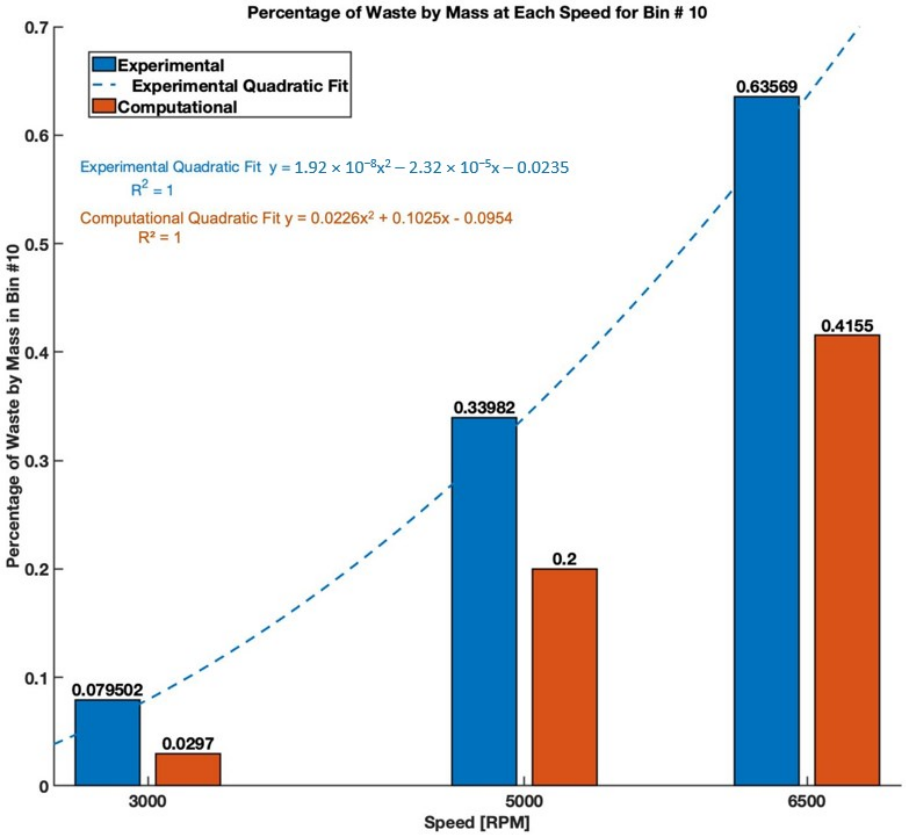

Figure 11. Percentage of mass in Bin #10 for each scenario.

The experimental procedure lacked data on an individual fragment level meaning the experimental mass had to be estimated based on the number of fragments in each bin and an average volume for each bin. In future studies, further work could include analyzing data for each individual fragment in the experimental methodology.

The experimental and computational curve fittings of the data in MATLAB® are reported in Figure 11. Both the experimental and computational data fit a quadratic equation. The equations do not match but they have the same form with an $R^2 = 1$. This quadratic equation seems to indicate that an increase in RPM quadratically augments the percentage of waste by mass of the mill. However, it is important to note that further study in determining the accuracy of this relationship is needed. In addition, it is unknown to the authors of this study if this relationship is transferable to a large production scale.

Although, the experimental and computational models do not highlight the exact same equation or identical particle size distribution by bin, both the experimental and computational results highlight the same trend, thus confirming the ability of SPH and the JH-2 material model to mimic the complex behavior of glass milling in a manufacturing production setting.

4. Conclusions

The primary conclusion from this study is that SPH, when used with the JH-2 material constitutive model, captures the fracture of soda-lime glass during the dynamic events of a milling process. The impacts during the milling process were enough to dislodge the individual particles from the kernel domain and to induce the fracture events. The output size distributions of the milling models matched the shape of the output size distributions found experimentally with the lab mill and Camsizer. The p-values for each

of the distributions at the various operating speeds were all above 0.05 indicating that the datasets obtained belong to the same distribution, and that the computational models provide an accurate representation of the milling process. In addition, the material bulk behavior for the JH-2 constitutive model was able to replicate the behavior of soda-lime glass under multiple loading scenarios. The low strain-rate dependence of the material allows the constitutive model to handle both ballistic and quasi-static loading conditions. For materials with a higher strain-rate dependence, the JH-2 constitutive model would not exhibit the correct behavior under quasi-static loading scenarios, as it is designed for high strain-rate scenarios.

The secondary conclusion of the study was that the 3000 RPM milling speed produced an output distribution with less waste product, as shown by the material accumulated in Bin #10 shown in Figure 11. The experimental testing revealed that the 3000 RPM operation produced the least amount of waste product at 14%. As the speed increased, the waste product of the milling process increased to 28 and 36%, respectively, for the 5000 RPM and 6500 RPM lab mill operations. The amount of waste in Bin #10 (Figure 11) showed a quadratic trend for both the experimental and computational results. It should also be considered that 3000 RPM might not be the optimal operating speed as particles can also be too big to continue through the manufacturing process. Further studies will need to be performed to identify the optimal operating speed that produces the most particles within a desired size range.

Author Contributions: Conceptualization, M.M.; methodology, J.A. and J.P.; software, J.A.; validation, M.C.F.B.; formal analysis, J.A., J.P., M.M., M.C.F.B. and C.G.M.; investigation, J.A., J.P. and M.M.; resources, M.M.; writing—original draft, J.A. and M.M.; writing—review and editing, M.M., M.C.F.B. and C.G.M.; supervision, M.M., M.C.F.B. and C.G.M. All authors have read and agreed to the published version of the manuscript.

Funding: This work was supported by Potters Industries LLC., under Clarkson University Master Collaboration Agreement Grant No. 22-01.

Data Availability Statement: The original contributions presented in the study are included in the article, further inquiries can be directed to the corresponding author.

Acknowledgments: The authors would like to acknowledge the valued contribution of Andy Gray for guidance on the use of the Camsizer.

Conflicts of Interest: The authors declare no conflicts of interest.

References

1. Kurkjian, C.R. From griffith flaws to perfect fibers a history of glass research. *J.-Non-Cryst. Solids* **1985**, *73*, 265–271. [CrossRef]
2. Burghardt, T.E.; Ettinger, K.; Köck, B.; Hauzenberger, C. Glass beads for road markings and other industrial usage: Crystallinity and hazardous elements. *Case Stud. Constr. Mater.* **2022**, *17*, e01213. [CrossRef]
3. Burghardt, T.E.; Pashkevich, A.; Babić, D.; Mosböck, H.; Babić, D.; Żakowska, L. Microplastics and road markings: The role of glass beads and loss estimation. *Transp. Res. Part Transp. Environ.* **2022**, *102*, 103123. [CrossRef]
4. Basdeki, M.; Apostolopoulos, C. The Effect of Shot Blasting Process on Mechanical Properties and Anti-Corrosive Behavior of Steel Reinforcement. *Metals* **2022**, *12*, 275. [CrossRef]
5. Pelfrene, J.; Van Dam, S.; Sevenois, R.; Gilabert, F.; Van Paepegem, W. Fracture simulation of structural glass by element deletion in explicit FEM. *Chall. Glass Conf. Proc.* **2016**, *5*, 439–454.
6. Guo, X.; Li, M.; Luo, X.; Zhai, R.; Kang, R.; Jin, Z.; Guo, D. Smoothed-particle hydrodynamics investigation on brittle–ductile transition of quartz glass in single-grain grinding process. *Nanomanuf. Metrol.* **2020**, *3*, 299–306. [CrossRef]
7. Nordendale, N.A. Modeling and Simulation of Brittle Armors under Impact and Blast Effects. Ph.D. Thesis, Vanderbilt University, Nashville, TN, USA, 2013.
8. Chu, D.; Li, X.; Liu, Z.; Cheng, J.; Wang, T.; Li, Z.; Zhuang, Z. A unified phase field damage model for modeling the brittle-ductile dynamic failure mode transition in metals. *Eng. Fract. Mech.* **2019**, *212*, 197–209. [CrossRef]
9. Murugesan, M.; Jung, D.W. Johnson Cook material and failure model parameters estimation of AISI-1045 medium carbon steel for metal forming applications. *Materials* **2019**, *12*, 609. [CrossRef] [PubMed]
10. Naik, R.; Panda, S.; Racherla, V. Failure analysis of metal-polymer-metal sandwich panels with wire mesh interlayers: Finite element modeling and experimental validation. *Compos. Struct.* **2022**, *280*, 114813. [CrossRef]

11. Tajdari, M. Modeling of Brittle and Ductile Material Drilling Using Smoothed-Particle Hydrodynamics. Ph.D. Thesis, Texas A&M University, College Station, TX, USA, 2016.
12. Johnson, G.R.; Holmquist, T.J. An improved computational constitutive model for brittle materials. In Proceedings of the AIP Conference Proceedings, American Institute of Physics, Sausalito, CA, USA, 17–19 November 1994; Volume 309, pp. 981–984.
13. Meyland, M.J.; Nielsen, J.H. Ongoing research into the failure of glass at high strain-rates. In Proceedings of the Challenging Glass Conference 7: International Conference on the Architectural and Structural Application of Glass, Ghent, Belgium, 18–19 June 2020.
14. *ASTM C1499*; Standard Test Method for Monotonic Equibiaxial Flexural Strength of Advanced Ceramics at Ambient Temperature. ASTM: West Conshohocken, PA, USA, 2019.
15. Tan, S.; Long, S.; Yao, X.; Zhang, X. An improved material model for loading-path and strain-rate dependent strength of impacted soda-lime glass plate. *J. Mater. Res. Technol.* **2021**, *15*, 1905–1919. [CrossRef]
16. Cole-Palmer. IKA 2836001 Continuous Feed Grinding Drive, 115 VAC/60 Hz. Available online: https://www.coleparmer.com/i/ika-2836001-continuous-feed-grinding-drive-115-vac-60-hz/0430130 (accessed on 22 September 2022).
17. Dassault Systèmes SE. *ABAQUS User's Manual*; Dassault Systèmes SE: Velizy-Villacoublay, France, 2022.
18. Swift Glass. Properties of Soda-Lime-SIlica Float Glass. 2023. Available online: http://www.swiftglass.com/assets/floatglass.pdf (accessed on 3 June 2023).
19. Dassault Systèmes SE. High-Velocity Impact of a Ceramic Target. 2022. Available online: https://help.3ds.com/2022/English/DSSIMULIA_Established/SIMACAEEXARefMap/simaexa-c-impactceramictarget.htm?contextscope=all (accessed on 3 June 2023).
20. TestResources. Mechanical and Product Testing Equipment & Applications Experts. Test Machines, Grips and Fixtures. 2022. Available online: https://www.testresources.net/ (accessed on 14 November 2022).
21. R-Core-Team. R: A Language and Environment for Statistical Computing. 2023. Available online: https://www.R-project.org/ (accessed on 15 December 2023).
22. Tukey, J.W. *Exploratory Data Analysis*; Addison-Wesley: Boston, MA, USA, 1977; Volume 2.
23. Kron Technologies. Chronos 2.1-HD High Speed Camera. 2023. Available online: https://www.krontech.ca/product/chronos-2-1-hd-high-speed-camera/ (accessed on 3 June 2023).
24. Microtrac MRB. Particle Size and Shape Analyzer (Camsizer 3D). 2023. Available online: https://www.microtrac.com/products/particle-size-shape-analysis/dynamic-image-analysis/camsizer-p4/ (accessed on 3 June 2023).
25. Schneider Company. Coefficient of Friction Reference Chart. 2023. Available online: https://www.schneider-company.com/coefficient-of-friction-reference-chart/ (accessed on 3 June 2023).
26. Massey, F.J., Jr. The Kolmogorov-Smirnov test for goodness of fit. *J. Am. Stat. Assoc.* **1951**, *46*, 68–78. [CrossRef]